

## Magnetic structure in the spin liquid $\text{Tb}_2\text{Ti}_2\text{O}_7$ induced by a [111] magnetic field: Search for a magnetization plateau

A. P. Sazonov,<sup>1,2,3,\*</sup> A. Gukasov,<sup>3</sup> H. B. Cao,<sup>4,3</sup> P. Bonville,<sup>5</sup> E. Ressouche,<sup>6</sup> C. Decorse,<sup>7</sup> and I. Mirebeau<sup>3</sup>

<sup>1</sup>*RWTH Aachen University, Institute of Crystallography, D-52056 Aachen, Germany*

<sup>2</sup>*Forschungszentrum Jülich GmbH, Jülich Centre for Neutron Science at MLZ, D-85747 Garching, Germany*

<sup>3</sup>*CEA, Centre de Saclay, DSM/IRAMIS/Laboratoire Léon Brillouin, F-91191 Gif-sur-Yvette, France*

<sup>4</sup>*Quantum Condensed Matter Division, Oak Ridge National Laboratory, Oak Ridge, Tennessee 37831, USA*

<sup>5</sup>*CEA, Centre de Saclay, DSM/IRAMIS/Service de Physique de l'Etat Condensé, F-91191 Gif-sur-Yvette, France*

<sup>6</sup>*SPSMS, UMR-E CEA/UJF-Grenoble 1, INAC, F-38054 Grenoble, France*

<sup>7</sup>*ICMMO UMR 8182, Université Paris-Sud, F-91405 Orsay, France*

(Received 21 June 2013; published 26 November 2013)

We have studied the field-induced magnetic structures of  $\text{Tb}_2\text{Ti}_2\text{O}_7$  pyrochlore by single-crystal neutron diffraction under a field applied along the [111] axis, up to  $H = 12$  T and down to  $T = 40$  mK. We refined the magnetic structures with  $\mathbf{k} = \mathbf{0}$  propagation vector by performing a symmetry analysis in the space group  $R\bar{3}m$ , reducing the number of free parameters to three only. The Tb moments gradually reorient towards the field direction, keeping close to a “3-in, 1-out / 1-in, 3-out” spin structure (magnetic space group  $R\bar{3}m'$ ) in the whole measured field range 0.05–12 T. Our results rule out the “all-in/all-out” structure previously proposed and do not support the existence of a magnetization plateau. We perform a quantitative comparison with mean-field calculations and we propose the presence of a low-temperature dynamic symmetry breaking of the local trigonal symmetry, akin to a dynamic Jahn-Teller effect, i.e., preserving the overall cubic symmetry. We discuss the possible origin of this off-diagonal mixing term in the crystal field Hamiltonian in terms of quadrupole-quadrupole interaction or magnetoelastic effects.

DOI: [10.1103/PhysRevB.88.184428](https://doi.org/10.1103/PhysRevB.88.184428)

PACS number(s): 71.27.+a, 61.05.fm, 75.25.-j

### I. INTRODUCTION

Spin ices are geometrically frustrated magnets, which support exotic ground states and excitations.<sup>1,2</sup> They are observed in rare-earth pyrochlores such as  $R_2\text{Ti}_2\text{O}_7$  ( $R = \text{Ho}, \text{Dy}$ ), where the  $R$  moments are situated on a lattice of corner sharing tetrahedra, and which combine an effective ferromagnetic interaction between the  $R$  moments with a local Ising anisotropy of the  $R$  ion. The zero-field magnetic ground state of the spin ices has an extensive degeneracy arising from topological constraints, which also governs the positions of protons of water molecules in real ice. Recently, intensive research started studying the role of quantum fluctuations in the spin-ice regime.<sup>3,4</sup> Quantum spin-ice (QSI) or quantum spin-liquid (QSL) phases are predicted, involving tunneling between different spin or charge ice configurations. Such states could be expected in rare-earth pyrochlores under reduced local anisotropy or for low effective spin values, but none of them have been fully ascertained in a real material yet.

$\text{Tb}_2\text{Ti}_2\text{O}_7$  is a potential candidate for such states. Initial experiments performed in 1999 suggested a classical spin-liquid (SL) behavior, akin to a cooperative paramagnet where strongly correlated magnetic moments fluctuate down to 50 mK at least.<sup>5</sup> Since then, a huge number of studies have been devoted to this compound. Very recently, a transition from this SL state to a mesoscopic antiferromagnetic (AF) state with  $\mathbf{k} = (\frac{1}{2}, \frac{1}{2}, \frac{1}{2})$  propagation vector was observed in powdered off-stoichiometric samples, tuned by a minute change of the Tb concentration.<sup>6</sup> This static AF order coexists with the SL fluctuations since it involves a tiny ordered moment ( $\sim 0.1 \mu_B$ ). It extends over a finite correlation length, and disappears at about 400 mK. In single crystals, elongated

diffuse spots centered at half-integer Bragg peak positions were also recently observed by several groups,<sup>7-9</sup> using either elastic scattering or diffuse scattering of polarized neutrons. These recent observations reconcile different experimental results concerning the  $\text{Tb}_2\text{Ti}_2\text{O}_7$  ground state, but their origin as well as that of the SL fluctuations remains a matter of debate, after more than 12 years of investigation.

A crucial point concerns the determination of a suitable energy interaction scheme for  $\text{Tb}_2\text{Ti}_2\text{O}_7$ . It is now well agreed upon<sup>10-12</sup> that this scheme should involve, at least, a proper description of the  $\text{Tb}^{3+}$  crystal field, anisotropic first-neighbor exchange interaction between Tb moments, and dipole-dipole interactions. Starting from this basis, it was first of all suggested that, unlike classical spin ices, the  $\text{Tb}_2\text{Ti}_2\text{O}_7$  crystal field scheme allows some admixture of excited crystal field levels into the ground state doublet.<sup>13,14</sup> Such an admixture may renormalize the exchange interactions of an unfrustrated antiferromagnet with local Ising anisotropy, rendering them effectively ferromagnetic, which led the authors to call  $\text{Tb}_2\text{Ti}_2\text{O}_7$  a quantum spin ice. The ground state found in this approach is, however, an ordered spin ice (OSI) with  $\mathbf{k} = \mathbf{0}$  propagation vector, which is actually observed in  $\text{Tb}_2\text{Sn}_2\text{O}_7$  (Ref. 15) but not in  $\text{Tb}_2\text{Ti}_2\text{O}_7$ . Alternatively, a symmetry breaking of the local trigonal symmetry at the rare-earth site, inducing a two-singlet crystal field ground state for the non-Kramers  $\text{Tb}^{3+}$  ion, was proposed to be the source of the SL fluctuations.<sup>16,17</sup> Such a model indeed predicts a SL phase in mean-field approximation and it accounts for the existence of a low-energy line in the inelastic neutron spectra. The existence of this inelastic line, initially hotly debated, has now been confirmed on safe grounds by several groups.<sup>9,16-19</sup> Very recently, it was shown to have an anisotropic spectral

weight with both quasielastic and dispersive components, thanks to polarized inelastic neutron scattering.<sup>20</sup> However, the distortion associated with the symmetry breaking, inferred from critical scattering x-ray measurements,<sup>21</sup> has not been observed at a macroscopic scale. Moreover, the static AF correlations<sup>9,16</sup> observed below 400 mK cannot be understood by the two-singlet model treated in mean field. Nevertheless, we believe that a part of the physical truth about the ground state in  $\text{Tb}_2\text{Ti}_2\text{O}_7$  resides in the two-singlet model, and we shall use it in the following to make comparisons with the experimental data.

A way to investigate the ground state is to perturb it by a magnetic field  $H$ . Especially, applying the field along a local [111] anisotropy axis should provide a stringent test of the theories. Indeed, for  $H \parallel [111]$ , the quantum spin-ice model predicts a magnetization plateau<sup>22</sup> as in spin ices, whereas the two-singlet model does not.<sup>23</sup> This plateau is, however, expected to be tiny, with anomalies in fields of about 100 mT, occurring at very low temperatures, typically below 100 mK. Several attempts to observe this plateau have been made recently by magnetic measurements or muon spin resonance,<sup>24–27</sup> with controversial results. No evidence of a plateau was found in the field dependence of the static magnetization, but anomalies in the ac susceptibility were detected at very low field and low temperature, well below the “transition” observed around 400 mK in zero field by specific heat and neutron scattering.<sup>6,28</sup> From the magnetization data of Ref. 24, a phase diagram was drawn and a microscopic spin structure of the type “all-in/all-out” was proposed, fully different from the “2-in, 2-out” local structure expected for a spin ice.

In  $\text{Tb}_2\text{Ti}_2\text{O}_7$ , magnetic long-range order (LRO) is induced by an applied field. This LRO is clearly seen by the onset of a magnetic contribution to the Bragg peaks of the face-centered cubic crystal structure with the  $\mathbf{k} = \mathbf{0}$  propagation vector, or by antiferromagnetic Bragg peaks of the simple cubic lattice with the  $\mathbf{k} = (0,0,1)$  propagation vector. Up to now, most of the in-field neutron diffraction data<sup>29,30</sup> were obtained for  $H \parallel [110]$ . In this configuration, a symmetry analysis allows one to determine the individual moment values and orientations of these complex noncollinear spin structures. This microscopic analysis emphasizes original field effects, invisible in the evolution of the average magnetization, such as a field-induced spin melting<sup>31</sup> and a double-layered monopolar order.<sup>32</sup> For  $H \parallel [111]$ , earlier neutron data<sup>33</sup> also showed the onset of LRO but the magnetic structure was not determined.

In this work, we have performed neutron diffraction measurements in a  $\text{Tb}_2\text{Ti}_2\text{O}_7$  single crystal to solve the magnetic structures for  $H \parallel [111]$  and to study the potential occurrence of a magnetization plateau. The experimental setup is described in Sec. II. At 300 mK, we collected a hundred Bragg reflections for selected fields in a large field range 0.05–12 T. We refined our data collections using symmetry analysis (Sec. III), yielding a precise determination of the field induced magnetic structures. Our results show a continuous evolution of the moment orientations with increasing field, fully consistent with the average magnetization, and close to the so-called “3-in, 1-out / 1-in, 3-out” spin structure in the whole field range ( $H > 0.05$  T) where it could be determined (Sec. IV). This picture rules out the all-in/all-out structure previously proposed.<sup>24</sup> Searching for a magnetization plateau,

we also accurately measured the field dependence of some selected Bragg peaks at 40 mK by scanning the magnetic field. We found no evidence of a magnetization plateau. In Sec. V, we compare the field evolution of the magnetic structure with that predicted by a mean-field (MF) treatment, including or not the off-diagonal mixing term phenomenologically assimilated to a dynamic distortion. We show that this term is needed to account for the data in applied field. In Sec. VI, we discuss our neutron results extensively with regard to the available microscopic descriptions and present some hypotheses to the origin of the quantum mixing term, in the light of very recent experiments.

## II. EXPERIMENT

A single crystal of  $\text{Tb}_2\text{Ti}_2\text{O}_7$  was grown from a sintered rod of the same nominal composition by the floating-zone technique, using a mirror furnace.<sup>30</sup> It was shaped as a cylinder of 3 mm diameter and 4 mm length. Unpolarized neutron-diffraction studies were performed on the CRG-CEA diffractometer D23 ( $\lambda = 1.2815 \text{ \AA}$ ) at the Institut Laue-Langevin, Grenoble.

The crystal structure was characterized in zero field at 300 mK. A total of 256 Bragg reflections with  $\sin \theta / \lambda \lesssim 0.55 \text{ \AA}^{-1}$  were measured and 48 unique reflections were obtained by averaging equivalents ( $R_{\text{int}} = 0.06$ ), using the cubic space group  $Fd\bar{3}m$ . The program FULLPROF (Ref. 34) was used to refine one oxygen positional parameter, all the isotropic temperature factors, the scale factor and the isotropic extinction parameter, yielding an agreement factor  $R_F = 0.05$ . The extinction correction was found to be quite important, yielding a FULLPROF extinction parameter of 2.4(4) which resulted in up to 60% reduction in the intensity of the strongest reflections.

To study the magnetic structures at 300 mK we collected about 100 Bragg reflections for each field value  $H$ , in an angular range  $\sin \theta / \lambda \lesssim 0.53 \text{ \AA}^{-1}$ . The field was applied along a [111] direction with a small misalignment angle of  $0.7^\circ$  and field intensity was varied between 0.05 and 12 T. The refinement of the components of the  $\text{Tb}^{3+}$  magnetic moments with symmetry constraints described below was performed using the program FULLPROF. We also performed the field scans of selected Bragg peaks in the temperature range 40–300 mK to study possible anomalies at very low temperatures.

## III. MAGNETIC SYMMETRY ANALYSIS

As noticed in Ref. 33, for  $H \parallel [111]$  we observe a magnetic contribution to the peaks of the face-centered-cubic lattice only, showing that the magnetic structure is characterized by a propagation vector  $\mathbf{k} = \mathbf{0}$ . For a careful magnetic symmetry analysis, we carried out a systematic search based on the theory of representations proposed by Bertaut<sup>35</sup> and Izyumov.<sup>36</sup> It allows one to consider all possible models of magnetic structures with a given propagation vector consistent with a crystal structure of a given space group (SG). According to this method, the magnetic structure can be expressed via the basis vectors (functions) of the corresponding irreducible representations (IRs). To generate the IRs and their basis functions, we used the ISOTROPY software suite.<sup>37</sup>

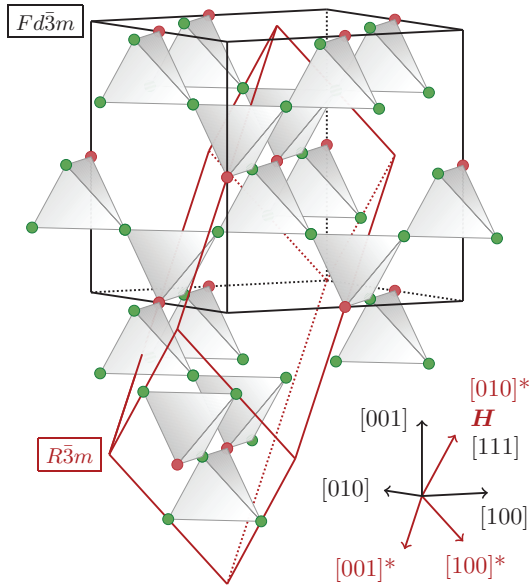


FIG. 1. (Color online) Transformation from the cubic  $Fd\bar{3}m$  (in black) to rhombohedral  $R\bar{3}m$  (in red) space group in  $Tb_2Ti_2O_7$ . Only the magnetic Tb atoms are shown for simplicity. Red and green cycles correspond to the  $3b$  sites (Tb1 atom) and  $9e$  sites (Tb2–Tb4 atoms) of SG  $R\bar{3}m$ , respectively.

Applying the field along one of the four threefold axes breaks the cubic  $Fd\bar{3}m$  symmetry and leads to a magnetic structure with lower symmetry than the underlying crystal structure. Therefore none of the four IRs predicted for the SG  $Fd\bar{3}m$  with  $\mathbf{k} = \mathbf{0}$ , are compatible with our data in an applied field.

We searched for new solutions in the rhombohedral SG  $R\bar{3}m$ , the highest subgroup of  $Fd\bar{3}m$  for which a homogeneous magnetization component induced by a field applied along  $[111]$  is invariant. The assumption of a rhombohedral symmetry is *a priori* valid in the paramagnetic region only (high temperature and high field) when the Zeeman energy overcomes the energy of the Tb–Tb interactions, so that a ternary symmetry of the moment values and orientations is imposed by the applied field. This point will be discussed below when comparing the results of the symmetry analysis with the mean-field calculations.

The transformation from the  $Fd\bar{3}m$  space group to the  $R\bar{3}m$  one is shown in Fig. 1. The new unit-cell parameters in  $R\bar{3}m$  are  $a^* = b^* = a\frac{\sqrt{2}}{2}$ ,  $c^* = a\sqrt{3}$ ,  $\alpha^* = \beta^* = 90^\circ$ , and  $\gamma^* = 120^\circ$ , where  $a$  is the cubic unit-cell parameter of the SG  $Fd\bar{3}m$ . Hereafter, the symbol  $*$  will be used to denote the lattice parameters, coordinates, and directions associated with the  $R\bar{3}m$  symmetry.

Assuming a rhombohedral symmetry leads to a splitting of the Tb  $16d$  Wyckoff position of  $Fd\bar{3}m$  into two crystallographically nonequivalent  $3b$  and  $9e$  positions in  $R\bar{3}m$ . The positions of the four Tb atoms within a primitive unit cell (in  $R\bar{3}m$ ) are defined in Table I as Tb1 ( $3b$  site) and Tb2–Tb4 ( $9e$  site) and shown in Fig. 1 by red and green colors, respectively. The Tb1 site corresponds to a  $Tb^{3+}$  atom whose local anisotropy axis  $[111]$  is parallel to  $\mathbf{H}$ , whereas the Tb2–Tb4 sites have

TABLE I. (Color online) The basis functions (magnetic modes) of the irreducible representation  $\Gamma_3$  in  $Tb_2Ti_2O_7$  for the  $3b$  sites (Tb1 atom) and  $9e$  sites (Tb2–Tb4 atoms) of the SG  $R\bar{3}m$ , associated with the propagation vector  $\mathbf{k} = \mathbf{0}$ . The magnetic Tb atoms are at the sites Tb1:  $(0,0,0)^*$ ; Tb2:  $(\frac{1}{6}, \frac{1}{3}, \frac{1}{3})^*$ ; Tb3:  $(-\frac{1}{3}, -\frac{1}{6}, \frac{1}{3})^*$ ; and Tb4:  $(\frac{1}{6}, -\frac{1}{6}, \frac{1}{3})^*$ . Labels of the magnetic modes are taken from the ISOTROPY software suite (Ref. 37).

IR	Mode	Atom	Components			Visualization
			x	y	z	
$\Gamma_3^{3b}$	$A_{2g}$	Tb1	0	0	1	
		Tb2	1	2	0	
$\Gamma_3^{9e}$	$B_g1$	Tb3	$\bar{2}$	$\bar{1}$	0	
		Tb4	1	$\bar{1}$	0	
		Tb2	0	0	1	

their local anisotropy axes  $[11\bar{1}]$ ,  $[\bar{1}11]$ , and  $[1\bar{1}1]$  at approx.  $109.47^\circ$  from the field.

As a result, the basis functions of the Tb1 and Tb2–Tb4 atoms are considered separately. Thus, the magnetic representations for the  $3b$  and  $9e$  sites of the SG  $R\bar{3}m$  are written as  $\Gamma_{Tb}^{3b} = 1\Gamma_3^{(1)} + 1\Gamma_5^{(2)}$  and  $\Gamma_{Tb}^{9e} = 1\Gamma_1^{(1)} + 2\Gamma_3^{(1)} + 3\Gamma_5^{(2)}$ , respectively. Here, the coefficients before the IR denote the number of times this representation is contained in the global magnetic representation, the superscript is the dimension of the IR, and the subscript is the number of the IR following the numbering scheme of Kovalev.<sup>38</sup> The basis vectors describing the Tb moments which transform according to IR  $\Gamma_1$  for  $9e$  sites (magnetic space group, MSG,  $R\bar{3}m$ ) can be ruled out on the basis of magnetization measurements as it does not allow the existence of a net ferromagnetic moment along the field direction  $[001]^*$  ( $[111]$  in cubic notation). The IR  $\Gamma_5$  for both Tb sites requires a further lowering of the magnetic symmetry (MSGs  $C2/m$ ,  $C2'/m'$ , and  $P\bar{1}$ ). Finally, only the one-dimensional representation  $\Gamma_3$  remains. Its basis functions are described and visualized for a single tetrahedron in Table I. For the  $3b$  sites, IR  $\Gamma_3$  allows the presence a ferromagnetic order along the field direction only (see the  $A_{2g}$  mode in Table I). In the case of the  $9e$  sites, its IR  $\Gamma_3$  allows both a net magnetization component along the field (see the  $B_g2$  mode in Table I) and triangular antiferromagnetic order in the plane perpendicular to the field (see the  $B_g1$  mode in Table I). The combination of these  $A_{2g}$ ,  $B_g1$ , and  $B_g2$  magnetic modes with their corresponding coefficients ( $U$ ,  $V$ ,  $V_z$ ) leads to the components  $M_x$ ,  $M_y$ , and  $M_z$  of a magnetic moment vector shown in Table II. Thus, the Tb magnetic moments at  $3b$  and  $9e$  sites can be varied separately within the MSG  $R\bar{3}m'$ .

To summarize, one parameter  $U$  for Tb at the  $3b$  site and two other parameters  $V$  and  $V_z$  for the  $9e$  sites are required

TABLE II. The  $M_x$ ,  $M_y$ , and  $M_z$  components of the magnetic moment for the Tb sites described in Table I. The coefficients of the  $A_{2g}$ ,  $B_g1$ , and  $B_g2$  magnetic modes (see Table I) of IR  $\Gamma_3 / \text{MSG } R\bar{3}m'$  are  $U$ ,  $V$ ,  $V_z$ , respectively.

IR	Atom	$M_x$	$M_y$	$M_z$
$\Gamma_3^{3b}$	Tb1	0	0	$U$
$\Gamma_3^{9e}$	Tb2	$V$	$2V$	$V_z$
	Tb3	$-2V$	$-V$	$V_z$
	Tb4	$V$	$-V$	$V_z$

to fully describe the magnetic structure of  $\text{Tb}_2\text{Ti}_2\text{O}_7$  with the above symmetry constraints. Thus, the symmetry analysis reduces the number of parameters to be refined from twelve in an unconstrained refinement (three for each of the four Tb moments in a tetrahedron) to three only.

#### IV. MAGNETIC STRUCTURE REFINEMENT

For each field value, the integrated intensities of the collected Bragg reflections were used to refine the components of the  $\text{Tb}^{3+}$  magnetic moments applying the symmetry constraints described in Sec. III. The parameters of the crystal structure were taken from the low-temperature measurements in zero field. In agreement with the above considerations, we found that among all possible irreducible representations predicted in the  $R\bar{3}m$  SG for  $\mathbf{k} = \mathbf{0}$ , only IR  $\Gamma_3 / \text{MSG } R\bar{3}m'$  (see Table II) provides a reliable description of the neutron diffraction data. The agreement factors  $R_F$  are about 0.04. An example of a typical fit is shown in Fig. 2 (left panel).

The field variations of the modulus of the Tb moments, of their polar ( $\theta$ ) and azimuthal ( $\varphi$ ) angles in the cubic

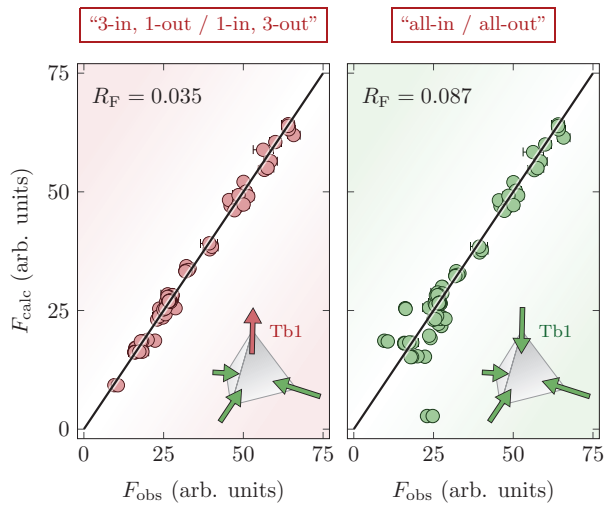


FIG. 2. (Color online) Typical example of the agreement between the calculated,  $F_{\text{calc}}$ , and experimentally measured,  $F_{\text{obs}}$ , Bragg intensities for  $\text{Tb}_2\text{Ti}_2\text{O}_7$ . Experimental data were collected at  $T = 300$  mK and  $H = 1$  T applied along the  $[111]$  direction. The magnetic structure refinement was performed by using the symmetry constraints described in Sec. III within the “3-in, 1-out / 1-in, 3-out” (left panel) and “all-in/all-out” (right panel) magnetic structures, respectively. The difference between the structures for a single tetrahedron is illustrated in the insets.

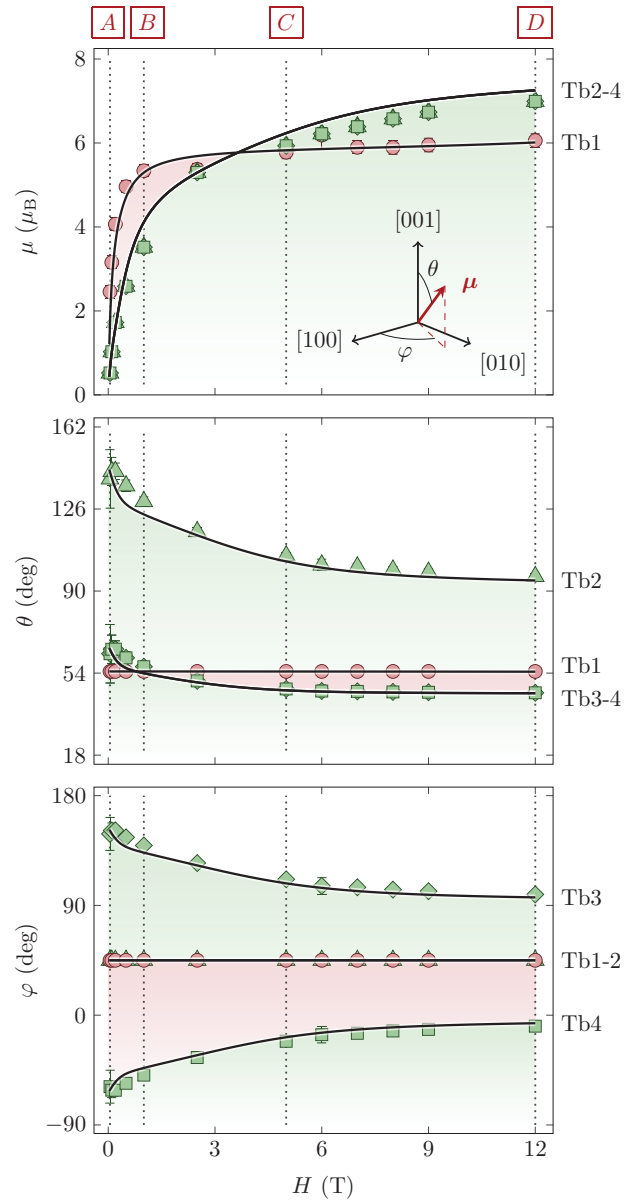


FIG. 3. (Color online) Field dependence of the angles and magnitudes of the Tb magnetic moments in  $\text{Tb}_2\text{Ti}_2\text{O}_7$  at 300 mK with  $\mathbf{H} \parallel [111]$ . Error bars are smaller than the symbol size if not given. The angles  $\varphi$  and  $\theta$  of a given moment  $\mu$  are defined at the upper inset in spherical coordinates. The solid lines are the mean-field calculations in Model II  $b$  (quantum mixing with dynamic Jahn-Teller effect), as described in Sec. V. The magnetic structures corresponding to the fields marked with “A”, “B”, “C”, and “D” (vertical dotted lines) are shown in Figs. 4 and 5 and described in the text.

frame, are presented in Fig. 3. The symbols correspond to the experimental values, determined by using the symmetry constraints (IR  $\Gamma_3 / \text{MSG } R\bar{3}m'$ , Sec. III), whereas the solid lines refer to the mean-field calculations (Model II, Sec. V). The data points for the Tb1 site are in red, whereas those for the Tb2–Tb4 sites are in green.

In Fig. 4, the moment orientations deduced from the refinements are drawn for different field values as the field increases from 0.05 to 12 T, focusing on a single tetrahedron. Figure 5 shows an extended plot of the magnetic lattice for

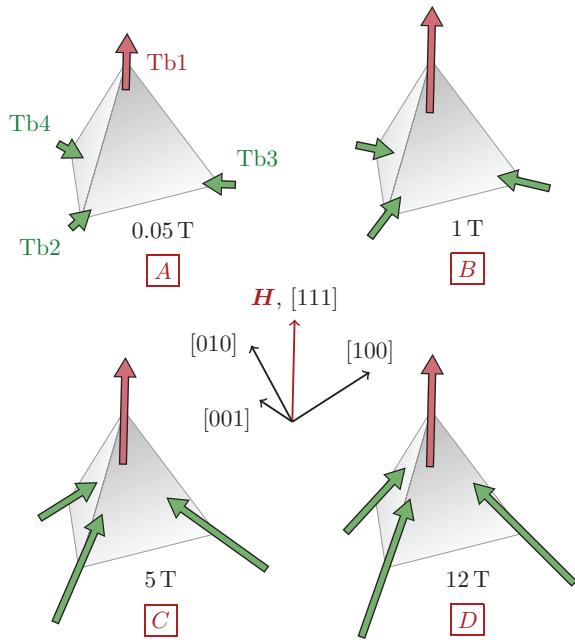


FIG. 4. (Color online) Field dependence of the Tb magnetic moments of  $\text{Tb}_2\text{Ti}_2\text{O}_7$  at 300 mK under  $\mathbf{H} \parallel [111]$ , for typical field values (cases A to D in Fig. 3). Only a single tetrahedron is shown for simplicity.

$H = 1$  T. For this field value, all Tb moments are aligned close to their local  $\langle 111 \rangle$  axes.

We first notice that in the whole field range where we collected data, the so-called 3-in, 1-out / 1-in, 3-out structure is stabilized (Fig. 4), with three moments (Tb2–Tb4, in green) pointing towards the center of the tetrahedron, and one moment (Tb1, in red) pointing out, or the reverse. Thus, even at the lowest field of 0.05 T, we can exclude the all-in/all-out magnetic structure proposed in Ref. 24. Such a structure obeys the symmetry analysis described above with the same IR as found experimentally but with different moment orientations, yielding a much worse agreement factor (see Fig. 2, right panel). According to the significance test on the crystallographic  $R$  factor,<sup>39</sup> the all-in/all-out structure at all the

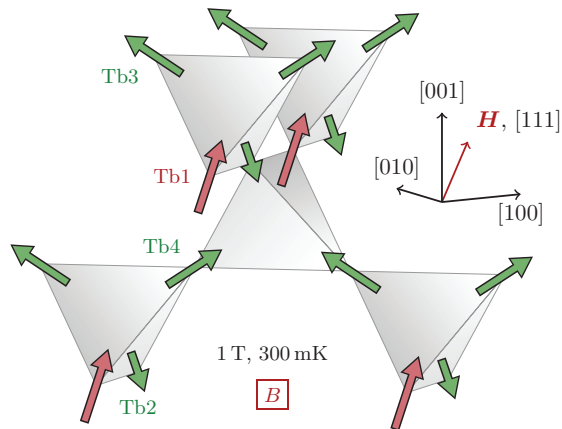


FIG. 5. (Color online) Field-induced magnetic structure of  $\text{Tb}_2\text{Ti}_2\text{O}_7$  with  $\mathbf{k} = \mathbf{0}$  propagation vector, stabilized for a field of 1 T along the  $[111]$  direction (case B in Fig. 3).

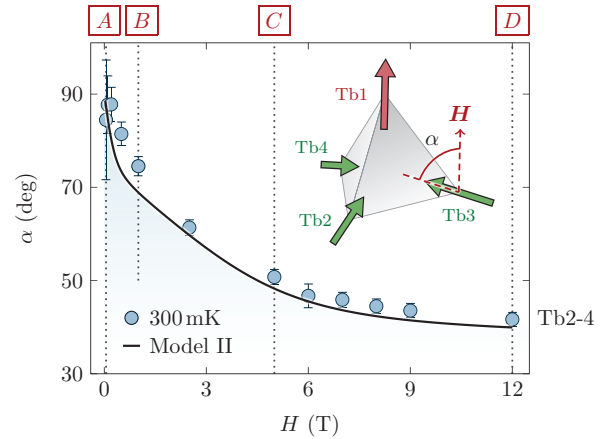


FIG. 6. (Color online) Field variation of the angle  $\alpha$  (see the inset) between the Tb2–Tb4 magnetic moments and the applied field  $\mathbf{H} \parallel [111]$ , as deduced from the refinement of the single-crystal neutron diffraction data with symmetry analysis (see Sec. III). Error bars are smaller than the symbol size if not given. The solid line is the mean-field calculations in Model II  $b$  (quantum mixing with dynamic Jahn-Teller effect), as described in Sec. V. The magnetic structures corresponding to the fields marked with “A”, “B”, “C”, and “D” (vertical dotted lines) are shown in Figs. 4 and 5.

measured fields can be rejected at a level of less than 0.005, i.e., with a confidence of more than 99.5%.

When the field increases, the Tb2–Tb4 moments slowly rotate from directions close to perpendicular to the applied field towards the field direction  $[111]$ . The angle  $\alpha$  between these moments and the applied field is plotted versus the field in Fig. 6. Thus the ferromagnetic component of the Tb2–Tb4 moments increases for two reasons: The moments rotate and their magnitudes increase with increasing field. At 12 T these moments still strongly deviate, by about  $42^\circ$ , from the field direction  $[111]$ . As for the Tb1 moments, they are always collinear to the field, according to the symmetry constraints described in Sec. III.

From our experimental neutron diffraction data, we can extract the magnetization of  $\text{Tb}_2\text{Ti}_2\text{O}_7$  and compare it to its determination by bulk magnetic measurements.<sup>24,25</sup> As seen in Fig. 7, both quantities are in good agreement, which is an important check of the robustness and consistency of our analysis and which ensures that all the experimental corrections have been done properly. In the measured field range, there is almost no variation of the magnetization between 300 and 80 mK. We note, however, a minor difference in  $M(H)$  below 2 T (see Fig. 8) when compared the data from Refs. 24 and 25, which may be a sample-dependent effect due to different demagnetization fields.

## V. MEAN-FIELD MODEL

Before computing the field evolution of the magnetic structure in  $\text{Tb}_2\text{Ti}_2\text{O}_7$  for  $\mathbf{H} \parallel [111]$ , one can first try to reproduce the magnetization curves down to very low temperature. The minimal Hamiltonian includes the trigonal crystal field, the Zeeman interaction, and Tb–Tb interactions, i.e., anisotropic exchange and dipole-dipole coupling. The zero-field ground state is then either an ordered spin-ice or an antiferromagnetic

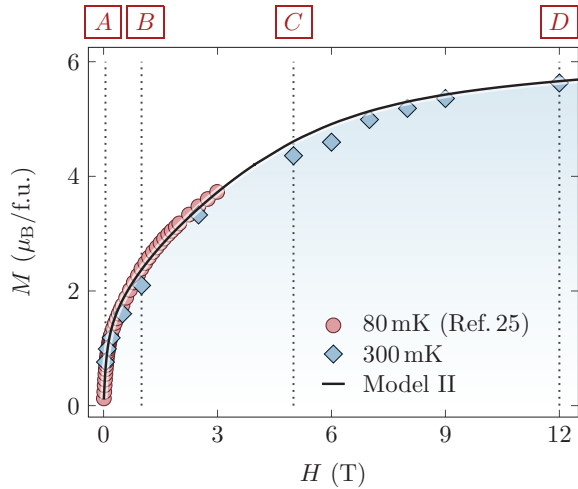


FIG. 7. (Color online) Field dependence of the magnetization  $M$  of  $\text{Tb}_2\text{Ti}_2\text{O}_7$  under  $\mathbf{H} \parallel [111]$  measured at 80 mK (red circles) according to Ref. 25. Blue diamonds correspond to the magnetization extracted from our neutron diffraction data at 300 mK. Error bars are smaller than the symbol size if not given. The solid line is the mean-field calculations with quantum mixing (Model II) as described in Sec. V. The magnetic structures corresponding to the fields marked with “A”, “B”, “C”, and “D” (vertical dotted lines) are shown in Figs. 4 and 5.

phase, depending on parameters, with a transition temperature around 1 K for parameter values relevant to  $\text{Tb}_2\text{Ti}_2\text{O}_7$ . This approach we call Model I in the following. If one adds to the crystal field Hamiltonian an off-diagonal mixing term arising at low temperature, as explained in detail in Ref. 16, then a spin-liquid phase emerges in a certain domain of exchange parameters. This approach is called Model II in the following. In both models, the Hamiltonian is treated in a mean-field self-consistent approximation and considers the 4 Tb sites in a tetrahedron. In the frame of Model II, an anisotropic exchange tensor  $\tilde{\mathcal{J}}_0 = \{-0.068, -0.200, -0.098\}$  K was derived for  $\text{Tb}_2\text{Ti}_2\text{O}_7$  in Ref. 16. The low-field part of the magnetization curves at 70 mK, 80 mK, and 2 K is shown in Fig. 8, together with the curves calculated using both models and the  $\tilde{\mathcal{J}}_0$  exchange tensor. Model I satisfactorily explains the field variation of the magnetization at 2 K, but it strongly overestimates the low-field magnetization at the lowest measured temperature 70–80 mK. The ground state of Model I with the  $\tilde{\mathcal{J}}_0$  exchange tensor is an OSI with transition temperature 600 mK. At 70–80 mK, the initial (vanishing field) magnetization value ( $2 \mu_B$ ) complies with the ice rules and is therefore worth 1/3 of the full ground state moment ( $\simeq 6 \mu_B$ ), but this remains far from the experimental data. This also confirms that the ordered spin-ice ground state stabilized in the QSI model,<sup>13,14</sup> which predicts  $\mathbf{k} = \mathbf{0}$  magnetic Bragg peaks (in zero field) as in  $\text{Tb}_2\text{Sn}_2\text{O}_7$ , is not the proper ground state of  $\text{Tb}_2\text{Ti}_2\text{O}_7$ .

Turning to Model II, we first note that, as recalled in the Introduction, there is presently no microscopic model able to account for all the features of the complex ground state of  $\text{Tb}_2\text{Ti}_2\text{O}_7$ . However, the fact that the virtual crystal field approach,<sup>13</sup> which implies a first-order perturbation of the crystal field, cannot describe the low-temperature

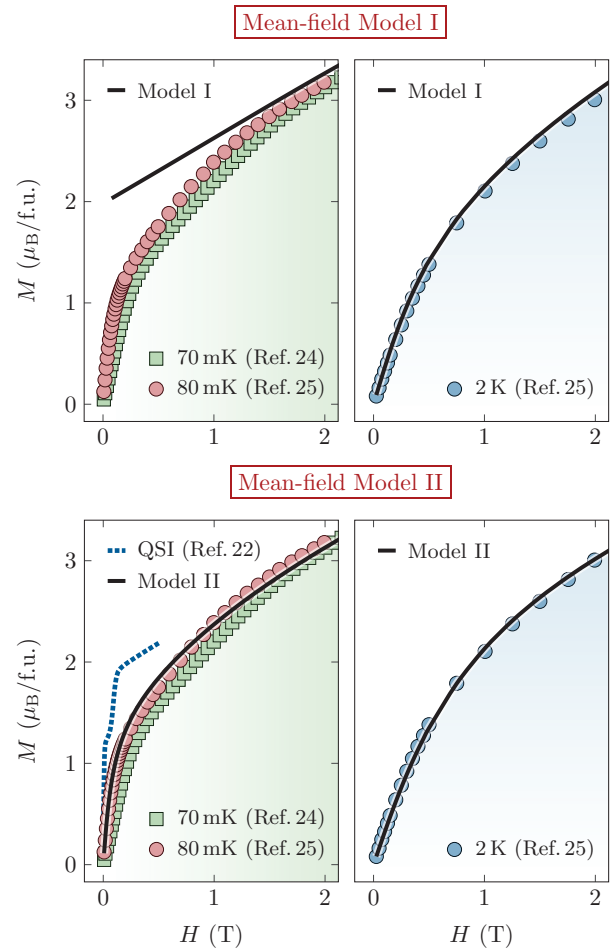


FIG. 8. (Color online) Low-field variations of the magnetization  $M$  of  $\text{Tb}_2\text{Ti}_2\text{O}_7$  under  $\mathbf{H} \parallel [111]$  measured at 70 mK (green squares) according to Ref. 24 and at 80 mK (red circles) and 2 K (blue circles) according to Ref. 25. The solid lines are mean-field calculations without quantum mixing term (Model I, upper panel) or with quantum mixing (Model II, lower panel) as described in Sec. V. The blue dotted line (lower panel) corresponds to the quantum spin-ice model (see Ref. 22).

magnetization, suggests that a zeroth-order perturbation is necessary. This implies a direct quantum mixing of the wave functions of the ground doublet induced by an off-diagonal term with respect to the generic Hamiltonian proposed for pyrochlores. The two-singlet model of Refs. 16 and 40 is the simplest rationalization of a direct quantum mixing. In  $\text{Tb}_2\text{Sn}_2\text{O}_7$ , it accounts for the energy and  $Q$  dependence of the maps measured by inelastic neutron scattering<sup>17</sup> quite correctly. In  $\text{Tb}_2\text{Ti}_2\text{O}_7$ , although it does not account properly for the spectral weight distribution of the spin fluctuations, it provides a reasonable basis for energy integrated measurements such as diffraction or diffuse scattering.<sup>16</sup> In the following, we examine the implications of Model II for our in-field neutron diffraction measurements.

A simple mixing term takes the form of a tetragonal distortion,<sup>21</sup> with equal probabilities that its axis  $OZ$  lies along one of the three fourfold  $\langle 100 \rangle$  directions. The overall cubic symmetry is therefore preserved. In case  $OZ$  is along  $[001]$ ,

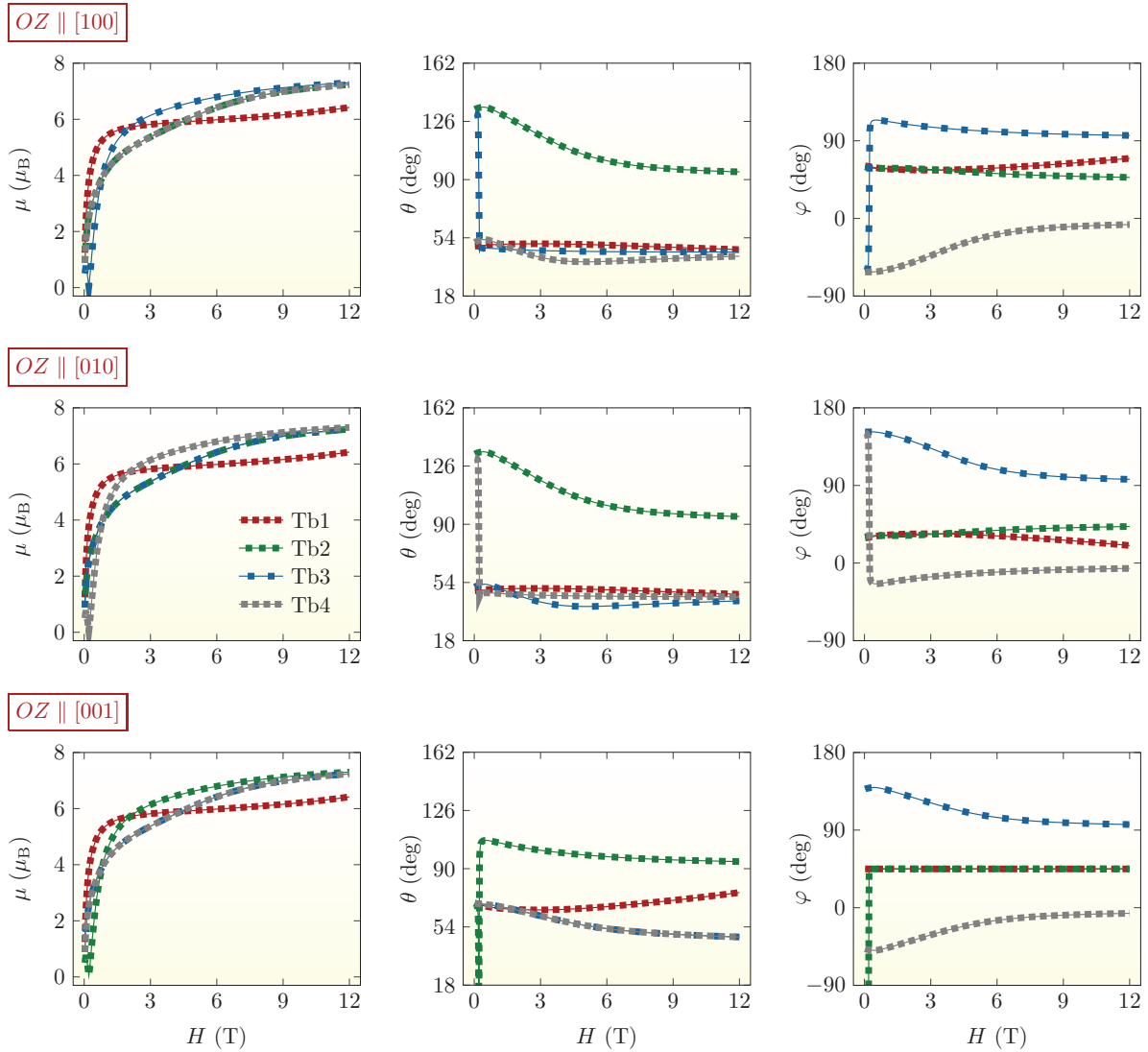


FIG. 9. (Color online) Calculated field variations, using Model II, of the modulus of the Tb moment, of its polar ( $\theta$ ) and azimuthal ( $\varphi$ ) angles in the cubic frame for the Tb1–Tb4 sites, and for the three possible distortion axes [100], [010], and [001].

the additional mixing term is

$$\mathcal{H}_Q = D_Q J_Z^2, \quad (1)$$

which is written, in the local frame with [111] as the  $z$  axis,

$$\mathcal{H}_Q = \frac{D_Q}{3} [2J_x^2 + J_z^2 + \sqrt{2}(J_x J_z + J_z J_x)]. \quad (2)$$

Since a fourfold axis makes the same angle with each of the local  $\langle 111 \rangle$  axes, Hamiltonian  $\mathcal{H}_Q$  has the same expression in four local frames of a tetrahedron. Inspection shows that the zeroth-order degeneracy lifting comes mainly from the last term in Eq. (2), i.e., the  $J_x J_z + J_z J_x$  operator. The value of the parameter  $D_Q$  was estimated to be 0.25 K from high-energy-resolution inelastic neutron scattering in zero magnetic field.<sup>16,29</sup> The magnetization computed using Model II with  $\mathcal{J}_0$  exchange and  $D_Q = 0.25$  K satisfactorily captures the low-field part (Fig. 8) as well as the whole magnetization curve up to 12 T (Fig. 7) in Tb<sub>2</sub>Ti<sub>2</sub>O<sub>7</sub> at very low temperature, thus allowing us to try and reproduce, on a more microscopic basis, the in-field magnetic structure.

The calculated spin structure using Model II depends on the particular axis  $OZ$  chosen for the mixing term. The predictions for the four Tb sites in terms of moment and angle values are shown in Fig. 9 independently for the three axes [001], [010], and [100]. The red curves correspond to the moment on the Tb1 site which has its threefold axis along  $\mathbf{H} \parallel [111]$ . The magnitude of the Tb1 moment quickly saturates above about 1 T and then does not significantly change up to 12 T, where the experimental value  $\mu_{\text{Tb1}} = 6.1(2) \mu_B$  is in good agreement with the calculated one. The calculated  $\mu(H)$  curves for the Tb1 moment are independent of the choice of the  $OZ$  axis, but  $\theta(H)$  and  $\varphi(H)$  are slightly different, especially at high field. By contrast, both moment values and orientations on the Tb2–Tb4 sites depend on the choice of the axis. Changing the axis from [001] to [010] or [100] induces permutations of the behaviors on the Tb2–Tb4 sites, in such a way that in each case two of three sites are swapped. In the following, we compare the predictions of Model II with the results of our neutron experiment in more detail.

## VI. DISCUSSION

The above analysis enlightens two points. First, a 3-in, 1-out / 1-in, 3-out magnetic structure is stabilized in the broad field range 0.05–12 T where we performed the data collections, with a gradual evolution of the moment values and orientations. Second, an energy term directly mixing the wave functions of the ground  $\text{Tb}^{3+}$  doublet, such as proposed by Model II, is necessary to account for the magnetization curve at low temperature. Considering the mixing Hamiltonian in terms of the Jahn-Teller effect, an equally probable distribution of the axis direction may be realized either at a microscopic or at a macroscopic level. Here we consider two variants, akin to the “single- $K$ ” (multidomain) and “multi- $K$ ” (single-domain) spin structures usually considered for a nonzero propagation vector. These variants can be associated with a static and a dynamic Jahn-Teller effect, respectively. We discuss here the interpretation of the neutron results with these two variants.

In the first variant (Model II  $a$ , static Jahn-Teller effect), we assume that the Jahn-Teller distortion is static, extends over a finite domain size, and that the domain orientations are equally distributed among the three cubic fourfold axes [100], [010], and [001]. The (unknown) domain size must be larger than the correlation length deduced from the width of the Bragg peaks (a few hundreds of Å). In this case, for each Bragg peak, one must average the contribution to the magnetic intensity from the three domains, and compare these averages to the measured Bragg intensities. This comparison does not require any constraint on the data treatment since the symmetry analysis and even the data refinement are not necessary.

In the second variant (Model II  $b$ , dynamic Jahn-Teller effect), we assume that the distortion remains long-range, but that its axis changes with time on each site between the three possible orientations. In this case, one should average the amplitude of the magnetic structure factor associated with the three possible axes on each Tb site. This corresponds to a vector sum of the magnetic moments calculated for each axis direction. Here, one can compare not only the Bragg intensities, but also the moment values and angles, derived from the refinement and the symmetry analysis, to the calculated values.

Calculations of the Bragg intensities show that the two variants never differ more than 5%, and are in excellent agreement with the experimental data in the whole field range. As an example, the field dependence of the  $(2\bar{2}0)$  Bragg reflection is shown in Fig. 10. Furthermore, the moment values and angles calculated assuming the second variant, Model II  $b$ , also agree very well with those deduced from the magnetic structure refinement, as shown in Figs. 3 and 6.

We conclude that the spin structures predicted assuming either static or dynamic Jahn-Teller effect are equally compatible with our neutron diffraction data in applied field. A dynamic Jahn-Teller effect could explain why no distortion has been observed on a macroscopic scale. The main drawback of the two-singlet model, appearing in zero field, remains present however. Namely, the mechanism slowing down the spin fluctuations (or softening the excitations) and yielding a dominant “elastic” signal in the neutron maps is unexplained. Up to now, no model succeeded to account for them, so that one should call for more complex mechanisms yielding cooperative effects.

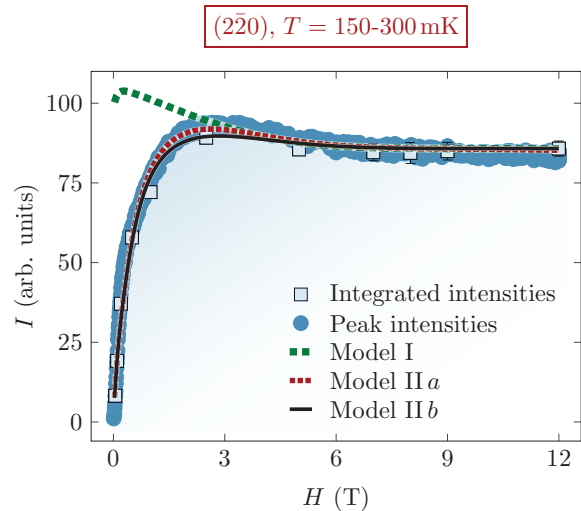


FIG. 10. (Color online) Field dependence of the  $(2\bar{2}0)$  Bragg reflection under  $\mathbf{H} \parallel [111]$ . The blue open squares correspond to the integrated intensities obtained with the data collections at 300 mK, and the blue closed circles are peak intensities measured during the field scans at 150–200 mK. Error bars are smaller than the symbol size if not given. The lines are mean-field calculations described in Sec. V. The green dashed line corresponds to Model I (no symmetry breaking). The red dotted and black solid lines are Model II  $a$  (quantum mixing with static Jahn-Teller effect) and Model II  $b$  (quantum mixing with dynamic Jahn-Teller effect), respectively. The two variants of the Model II yield the same result within less than 5% for all calculated Bragg peaks.

Their nature could be either intrinsic (quantum mixing on a larger scale than a single site, yielding a Jahn-Teller transition or quadrupolar ordering) or extrinsic (influence of disorder and further neighbor interactions, yielding a spin glass). Such mechanisms could restore a magnetic state in zero field instead of the nonmagnetic one found by the mean-field two-singlet model.

We also show in Fig. 11 the low-field variation of the peak intensities of some typical Bragg reflections, which

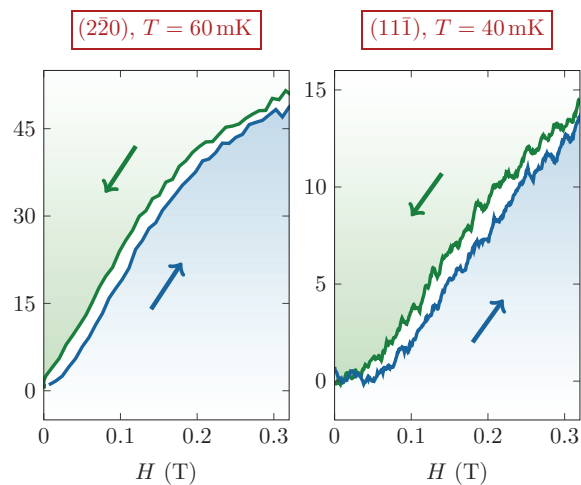


FIG. 11. (Color online) Field dependences of the intensity of the  $(2\bar{2}0)$  and  $(11\bar{1})$  magnetic Bragg reflections in  $\text{Tb}_2\text{Ti}_2\text{O}_7$  with  $\mathbf{H} \parallel [111]$  measured during field scans at 40–60 mK.



we measured down to 40 mK by scanning the field with great accuracy, searching for anomalies related to a potential magnetization plateau. We did not observe any anomalies in the field range predicted,<sup>22</sup> and the field variations of the Bragg peaks almost superimpose in the temperature range 40–300 mK. We therefore conclude that a magnetization plateau is quite unlikely. Given our experimental results, it should only occur in a very limited range of temperature and fields (below 40 mK and 0.2 T). Moreover, the predicted variation of the magnetization disagrees with the experimental one even above the plateau as shown in Fig. 8 (lower panel). We therefore attribute the anomalies and irreversibilities of the susceptibility and muon spin resonance ( $\mu$ SR) data<sup>24–26,41</sup> below 400 mK to a partial freezing of the Tb moments and not to the onset of a plateau. The small hysteresis of the field dependence of the Bragg peaks when cooling the sample in a magnetic field, which we did not investigate in detail, supports this interpretation.

Finally, we discuss possible origins for the zeroth-order quantum mixing which seems necessary in order to account for many low-temperature properties of  $\text{Tb}_2\text{Ti}_2\text{O}_7$ . In keeping with the Jahn-Teller picture, a two-ion quadrupole-quadrupole interaction naturally emerges from Hamiltonian in Eq. (2) since it can be written in terms of the rare-earth quadrupolar operators  $Q_{ij}$ , with their standard definitions, as

$$\mathcal{H}_Q = \frac{D_Q}{3} \left[ 2Q_{xx} + Q_{zz} + \frac{J(J+1)}{3} + 2\sqrt{2}Q_{xz} \right]. \quad (3)$$

As mentioned in Sec. V, the leading term yielding a zeroth-order splitting of the  $\text{Tb}^{3+}$  ground doublet is  $Q_{xz} = \frac{1}{2}(J_x J_z + J_z J_x)$ . Then, keeping only this term, the Hamiltonian in Eq. (3) can be seen as a Jahn-Teller driven quadrupole-quadrupole coupling treated in mean field, and it would be equivalent to

$$\mathcal{H}_{JT} = -g_Q \langle Q_{xz} \rangle Q_{xz}, \quad (4)$$

where  $g_Q$  is an interaction parameter. Such an energy term should lead to a quadrupolar transition, accompanied by a lack of standard long-range magnetic order, at a temperature  $T_Q$  depending on the interaction strength  $g_Q$ . The specific heat peak observed near 0.5 K for a certain degree of off-stoichiometry in  $\text{Tb}_2\text{Ti}_2\text{O}_7$  (Ref. 6) could correspond to such a transition.

Another possibility is that the state mixing would have its origin in the single-ion magnetoelastic coupling, known to be strong in  $\text{Tb}_2\text{Ti}_2\text{O}_7$  (Refs. 42–44). The magnetoelastic

Hamiltonian at the rare-earth site with  $D_{3d}$  symmetry, limited to second-order terms, also involves the  $Q_{xz}$  operator (usually called  $O_2^1$ ). Using the notations of Ref. 45, the relevant part of the magneto-elastic interaction is written as

$$\mathcal{H}_{m-el} = [(\epsilon_{xx} - \epsilon_{yy})B_{21}^{xx} + 2\epsilon_{xz}B_{21}^{zx}] Q_{xz}, \quad (5)$$

involving components of the strain tensor  $\tilde{\epsilon}$ . A resonant coupling of a phonon to the  $4f$  electrons can then occur through this interaction. The existence of such a coupling is suggested by very recent inelastic neutron scattering data showing a strong interaction between the acoustic phonon branch and the first crystal field excitation, leading to a hybrid vibronic mode.<sup>20,46</sup> Very recent measurements of the thermal conductivity in  $\text{Tb}_2\text{Ti}_2\text{O}_7$  concluded along the same line, i.e., that the acoustic phonon branch is strongly scattered at low temperature, resulting in a very low thermal conductivity.<sup>47</sup>

## VII. CONCLUSION

In conclusion, our single-crystal neutron diffraction data obtained in  $\text{Tb}_2\text{Ti}_2\text{O}_7$  with  $\mathbf{H} \parallel [111]$  show a continuous evolution of the field-induced magnetic structure, which keeps a “3-in, 1-out / 1-in, 3-out” arrangement in the whole field range up to 12 T; this invalidates both the magnetization plateau and the “all-in/all-out” spin structures previously proposed. Comparison with a mean-field model strongly supports the existence of a zeroth-order quantum mixing of the two states of the ground  $\text{Tb}^{3+}$  doublet, already inferred from inelastic neutron scattering, and occurring at low temperature. The evolution of the magnetization and magnetic structure deduced from our neutron diffraction data at 300 mK and in the field range 0.05–12 T, for  $\mathbf{H} \parallel [111]$ , are well accounted for by our model. Considering the quantum mixing in terms of the Jahn-Teller effect, the diffraction data are compatible with both a static and a dynamic effect. Other phenomena driven by the magnetoelastic interaction, such as quadrupolar ordering and/or hybrid electronic-phonon modes as recently observed, could possibly be simulated by the phenomenological quantum mixing presented here.

## ACKNOWLEDGMENTS

We thank S. Petit and J. Robert for useful discussions, and B. Grenier for her help during the experiment. The work of A. P. Sazonov and H. B. Cao was performed during their post-doc stay at the Laboratoire Léon Brillouin.

\*mail@sazonov.org; http://sazonov.org

<sup>1</sup>S. T. Bramwell and M. J. P. Gingras, *Science* **294**, 1495 (2001).

<sup>2</sup>C. Castelnovo, R. Moessner, and S. L. Sondhi, *Nature (London)* **451**, 42 (2008).

<sup>3</sup>O. Benton, O. Sikora, and N. Shannon, *Phys. Rev. B* **86**, 075154 (2012).

<sup>4</sup>L. Savary and L. Balents, *Phys. Rev. Lett.* **108**, 037202 (2012).

<sup>5</sup>J. S. Gardner, S. R. Dunsiger, B. D. Gaulin, M. J. P. Gingras, J. E. Greedan, R. F. Kiefl, M. D. Lumsden, W. A. MacFarlane,

N. P. Raju, J. E. Sonier, I. Swainson, and Z. Tun, *Phys. Rev. Lett.* **82**, 1012 (1999).

<sup>6</sup>T. Taniguchi, H. Kadowaki, H. Takatsu, B. Fåk, J. Ollivier, T. Yamazaki, T. J. Sato, H. Yoshizawa, Y. Shimura, T. Sakakibara, T. Hong, K. Goto, L. R. Yaraskavitch, and J. B. Kycia, *Phys. Rev. B* **87**, 060408 (2013).

<sup>7</sup>T. Fennell, M. Kenzelmann, B. Roessli, M. K. Haas, and R. J. Cava, *Phys. Rev. Lett.* **109**, 017201 (2012).

<sup>8</sup>S. Petit, P. Bonville, J. Robert, C. Decorse, and I. Mirebeau, *Phys. Rev. B* **86**, 174403 (2012).

- <sup>9</sup>K. Fritsch, K. A. Ross, Y. Qiu, J. R. D. Copley, T. Guidi, R. I. Bewley, H. A. Dabkowska, and B. D. Gaulin, *Phys. Rev. B* **87**, 094410 (2013).
- <sup>10</sup>M. Enjalran and M. J. P. Gingras, *Phys. Rev. B* **70**, 174426 (2004).
- <sup>11</sup>S. H. Curnoe, *Phys. Rev. B* **78**, 094418 (2008).
- <sup>12</sup>S. B. Lee, S. Onoda, and L. Balents, *Phys. Rev. B* **86**, 104412 (2012).
- <sup>13</sup>H. R. Molavian, M. J. P. Gingras, and B. Canals, *Phys. Rev. Lett.* **98**, 157204 (2007).
- <sup>14</sup>H. R. Molavian, P. A. McClarthy, and M. J. P. Gingras, arXiv:0912.2957.
- <sup>15</sup>I. Mirebeau, A. Apetrei, J. Rodriguez-Carvajal, P. Bonville, A. Forget, D. Colson, V. Glazkov, J. P. Sanchez, O. Isnard, and E. Suard, *Phys. Rev. Lett.* **94**, 246402 (2005).
- <sup>16</sup>P. Bonville, I. Mirebeau, A. Gukasov, S. Petit, and J. Robert, *Phys. Rev. B* **84**, 184409 (2011).
- <sup>17</sup>S. Petit, P. Bonville, I. Mirebeau, H. Mutka, and J. Robert, *Phys. Rev. B* **85**, 054428 (2012).
- <sup>18</sup>B. D. Gaulin, J. S. Gardner, P. A. McClarty, and M. J. P. Gingras, *Phys. Rev. B* **84**, 140402 (2011).
- <sup>19</sup>H. Takatsu, H. Kadowaki, T. J. Sato, J. W. Lynn, Y. Tabata, T. Yamazaki, and K. Matsuhira, *J. Phys.: Condens. Matter* **24**, 052201 (2012).
- <sup>20</sup>S. Guitteny, J. Robert, P. Bonville, J. Ollivier, C. Decorse, P. Steffens, M. Boehm, H. Mutka, I. Mirebeau, and S. Petit, *Phys. Rev. Lett.* **111**, 087201 (2013).
- <sup>21</sup>J. P. C. Ruff, B. D. Gaulin, J. P. Castellan, K. C. Rule, J. P. Clancy, J. Rodriguez, and H. A. Dabkowska, *Phys. Rev. Lett.* **99**, 237202 (2007).
- <sup>22</sup>H. R. Molavian and M. J. P. Gingras, *J. Phys.: Condens. Matter* **21**, 172201 (2009).
- <sup>23</sup>P. Bonville, S. Petit, I. Mirebeau, J. Robert, E. Lhotel, and C. Paulsen, arXiv:1302.6418.
- <sup>24</sup>S. Legl, C. Krey, S. R. Dunsiger, H. A. Dabkowska, J. A. Rodriguez, G. M. Luke, and C. Pfleiderer, *Phys. Rev. Lett.* **109**, 047201 (2012).
- <sup>25</sup>E. Lhotel, C. Paulsen, P. D. de Réotier, A. Yaouanc, C. Marin, and S. Vanishri, *Phys. Rev. B* **86**, 020410 (2012).
- <sup>26</sup>P. J. Baker, M. J. Matthews, S. R. Giblin, P. Schiffer, C. Baines, and D. Prabhakaran, *Phys. Rev. B* **86**, 094424 (2012).
- <sup>27</sup>L. Yin, J. S. Xia, Y. Takano, N. S. Sullivan, Q. J. Li, and X. F. Sun, *Phys. Rev. Lett.* **110**, 137201 (2013).
- <sup>28</sup>Y. Chapuis, A. Yaouanc, P. Dalmas de Réotier, C. Marin, S. Vanishri, S. H. Curnoe, C. Vâju, and A. Forget, *Phys. Rev. B* **82**, 100402 (2010).
- <sup>29</sup>K. C. Rule, J. P. C. Ruff, B. D. Gaulin, S. R. Dunsiger, J. S. Gardner, J. P. Clancy, M. J. Lewis, H. A. Dabkowska, I. Mirebeau, P. Manuel, Y. Qiu, and J. R. D. Copley, *Phys. Rev. Lett.* **96**, 177201 (2006).
- <sup>30</sup>H. Cao, A. Gukasov, I. Mirebeau, P. Bonville, and G. Dhahlenne, *Phys. Rev. Lett.* **101**, 196402 (2008).
- <sup>31</sup>A. P. Sazonov, A. Gukasov, I. Mirebeau, H. Cao, P. Bonville, B. Grenier, and G. Dhahlenne, *Phys. Rev. B* **82**, 174406 (2010).
- <sup>32</sup>A. P. Sazonov, A. Gukasov, I. Mirebeau, and P. Bonville, *Phys. Rev. B* **85**, 214420 (2012).
- <sup>33</sup>Y. Yasui, M. Kanada, M. Ito, H. Harashina, M. Sato, H. Okumura, and K. Kakurai, *J. Phys. Chem. Solids* **62**, 343 (2001).
- <sup>34</sup>J. Rodríguez-Carvajal, *Physica B* **192**, 55 (1993).
- <sup>35</sup>E. F. Bertaut, *Acta Crystallogr. A* **24**, 217 (1968).
- <sup>36</sup>Y. A. Izyumov and V. E. Naish, *J. Magn. Magn. Mater.* **12**, 239 (1979).
- <sup>37</sup>B. J. Campbell, H. T. Stokes, D. E. Tanner, and D. M. Hatch, *J. Appl. Crystallogr.* **39**, 607 (2006).
- <sup>38</sup>O. V. Kovalev, *Irreducible Representations of the Space Groups* (Gordon and Breach, New York, 1965).
- <sup>39</sup>W. C. Hamilton, *Acta Crystallogr.* **18**, 502 (1965).
- <sup>40</sup>K. C. Rule and P. Bonville, *J. Phys.: Conf. Ser.* **145**, 012027 (2009).
- <sup>41</sup>N. Tariq, N. A. Taisan, V. Singh, and J. D. Weinstein, *Phys. Rev. Lett.* **110**, 153201 (2013).
- <sup>42</sup>L. G. Mamsurova, K. S. Pigal'skii, and K. K. Pukhov, *Pis'ma Zh. Eksp. Teor. Fiz.* **43**, 584 (1986) [*JETP Lett.* **43**, 755 (1986)].
- <sup>43</sup>Y. Nakanishi, T. Kumagai, M. Yoshizawa, K. Matsuhira, S. Takagi, and Z. Hiroi, *Phys. Rev. B* **83**, 184434 (2011).
- <sup>44</sup>Y. Luan, Ph.D. thesis, University of Tennessee, 2011 (unpublished), [http://trace.tennessee.edu/utk\\_graddiss/993](http://trace.tennessee.edu/utk_graddiss/993)
- <sup>45</sup>V. V. Klekovkina, A. R. Zakirov, B. Z. Malkin, and L. A. Kasatkina, *J. Phys.: Conf. Ser.* **324**, 012036 (2011).
- <sup>46</sup>T. Fennell, M. Kenzelmann, B. Roessli, H. Mutka, J. Ollivier, M. Ruminy, U. Stuhr, O. Zaharko, L. Bovo, A. Cervellino, M. K. Haas, and R. J. Cava, arXiv:1305.5405.
- <sup>47</sup>Q. J. Li, Z. Y. Zhao, C. Fan, F. B. Zhang, H. D. Zhou, X. Zhao, and X. F. Sun, *Phys. Rev. B* **87**, 214408 (2013).